Pergamon

0020–7683(94)00300–9

ON THE DYNAMIC SHEAR RESISTANCE OF CERAMIC COMPOSITES AND ITS DEPENDENCE ON APPLIED MULTIAXIAL DEFORMATION

H. D. ESPINOSA

School of Aeronautics and Astronautics, Purdue University,
West Lafayette, IN 47907-1282, U.S.A.

Abstract—The high strain rate response of an AlN/AlN/Al composite manufactured by Lanxide Armor Products, has been studied by means of normal and pressure-shear plate impact experiments. A dramatic reduction in post yield shear strength, measured in these experiments, motivated the examination of the material response by using a microcracking multiple-plane model and a continuum elasto-viscoplastic constitutive model. Numerical simulations of the normal impact experiments do not support microcracking as the dominant inelastic mechanism at the early stages of inelasticity. By contrast, an elasto-viscoplastic description of the material behavior predicts the main features of the normal stress history. Nonetheless, the elasto-viscoplastic model cannot reproduce both the normal and the pressure-shear experiments with a single set of model parameters. The inadequacy of the continuum elasto-viscoplastic model seems to result from the *isotropic* flow assumption embodied in its formulation. The shear resistance measured in the pressure-shear experiments is adequately predicted by a multiple-plane model with a pressure and rate dependent flow mechanism. The agreement seems to hinge on the continuous shearing of the material in a micro-localized fashion; i.e. only one orientation becomes dominant and controls the inelastic shear deformation rate. This event does not occur in the normal impact configuration, in which the amount of inelasticity is primarily controlled by the elastic compressibility of the material. These findings explain the higher sensitivity to damage and microplasticity observed in the pressure-shear testing of ceramics and ceramic composites, as well as the softer material response recorded in this configuration. Although the mechanism used in the formulation of the multiple-plane model is microcracking, the implications discussed here are valid for other mechanisms in which the inelastic deformation is pressure dependent. The actual inelastic mechanism is still unknown. Therefore, plate impact experiments specially designed for post-test examination of the specimens are needed for its proper identification.

1. INTRODUCTION

The formulation of constitutive models capable of reproducing the inelastic events observed in ceramics and ceramic composites is essential to their technological application. In the case of ballistic applications, understanding of material response at high pressures and strain rates is a key aspect in the design of armor tiles (Shockey *et al.*, 1990). Plate impact experiments offer ideal conditions for the examination of the material behavior under such conditions. Nonetheless, differences encountered in the measured shear resistance of these materials, when both normal impact and pressure-shear experiments are conducted, indicate the need for detailed analyses of these experiments.

In an attempt to understand the ceramic resistance to penetration, Klopp and Shockey (1991) performed symmetric pressure-shear experiments on SiC plates and numerical simulations of the wave propagation event. By postulating a viscoplastic constitutive model, they concluded that the flow strength measured through pressure-shear experiments is much softer than the flow response of intact SiC ceramic measured by means of normal impact experiments (Kipp and Grady, 1989). Even more surprising is the fact that the measured dynamic shear resistance of SiC, by means of pressure-shear experiments, is even lower than that obtained for powder SiC ceramic, under quasi-static conditions (Johnson *et al.*, 1990). A similar behavior is reported in Curran *et al.* (1993) for AlN. In the analysis of the pressure-shear experiments, performed by Curran *et al.*, a micromechanical model for comminution and granular flow is postulated. Fragmentation during the early part of the test and subsequent flow of fully comminuted material is predicted by the model. In both

papers (Klopp and Shockey, 1991 ; Curran *et al.*, 1993) the authors mentioned the possibility of interface failure at the impact surface as another mechanism that could explain the lower shear strength measured in the pressure-shear experiments. Nonetheless, there is not experimental evidence supporting this failure mechanism. A more likely event that could lead to a misinterpretation of the experimental results would be the spallation of the boron carbide anvil plate, in the high strain rate configuration used in the testing of AlN, or the spallation of the SiC target in the case of the symmetric pressure-shear configuration used in the testing of SiC. Experimental evidence of spallation, when a pure shear state of stress develops in a brittle target plate, has been reported by Espinosa and Clifton (1991).

The purpose of this paper is to investigate the shear resistance of particulate ceramic composites and its dependence on applied multiaxial deformation. In particular we examine the role of the microstructure in the interpretation of the material behavior. Rather than postulating constitutive models which superimpose microfracture, void collapse, and plasticity (e.g. Rajendran, 1992), we investigate each mechanism independently. In this work we do not intend to build a model to provide the best fit of the experimental records; we plan to examine the relevance of each failure mechanism. Furthermore, the possibility of shear flow along preferred orientations and damage-induced anisotropy are studied by means of a multiple-plane model. The paper starts with a description of the tested material, an AlN/AlN/Al ceramic composite, followed by a discussion of relevant normal and pressure-shear experimental records. Some of these experiments have been presented in a previous paper (Espinosa and Clifton, 1991). As in the case of SiC and AlN, the shear resistance of the AlN/AlN/Al composite as measured in pressure-shear experiments, appears to be lower than the shear resistance inferred from normal impact experiments. It should be noted that in this study spallation of the anvil plate did not occur, implying that the source for the softer response of the material in pressure-shear may differ from the source present in the tests conducted on AlN and SiC ceramics. Clarification of this point is pursued by examining the material response through a micromechanical microcracking multiple-plane model and a continuum plasticity model incorporating softening, pressure and rate dependence. In the multiple-plane model postulated by Curran *et al.* (1993) emphasis is placed in the description of the material behavior upon fragmentation. However, the relative importance of the properties of comminuted and intact material in the penetration resistance of brittle materials is not known. Therefore, in this work the transition from intact to pulverized material is studied by means of the derived microcracking multiple-plane model. The paper ends with a discussion of the features revealed by the performed numerical simulations. The simulations show that the shear resistance measured in the pressure-shear experiments is adequately predicted by a multiple-plane model with a pressure and rate dependent flow mechanism. Furthermore, it is inferred that the agreement hinges on the continuous shearing of the material in a micro-localized fashion, i.e. only one orientation becomes dominant and controls the inelastic shear deformation rate. This event is not predicted by the numerical simulation of the normal impact configuration in which the amount of inelasticity is primarily controlled by the elastic compressibility of the material. These findings explain the higher sensitivity to damage and microplasticity observed in the pressure-shear testing of ceramics and ceramic composites, as well as the softer material response recorded in this configuration.

2. THE MATERIAL

An aluminum nitride–aluminum matrix reinforced by aluminum nitride particles (AlN/AlN/Al), which has been developed by Lanxide Armor Products, has been tested. Specifically, this composite material consists of aluminum nitride (AlN) reinforcement particles with a mean diameter of 3 μm and a matrix of AlN/Al, with AlN referred to as the reaction product. The density of the composite is 3.165 g cm^{-3}. This density is less than that for fully dense AlN, 3.26 g cm^{-3}, because the composite contains residual alloy. However, the small density difference is an indication of the predominant AlN phase, and therefore, an overall quasi-brittle response is expected. A fracture toughness $K_{IC} = 3.7$ $MPa\sqrt{m}$ has been measured.

The material is manufactured using the DIMOX™, directed metal oxidation process. The process starts with the formation of a porous preform of reinforcement particles held together with an added binder. The AlN/Al matrix growth involves the reaction of a molten aluminum alloy, Al–Sr–Si–Ni, in a nitrogen atmosphere. Under certain conditions of temperature and nitrogen pressure, the AlN reaction product grows outward from the original alloy surface. Molten aluminum alloys are drawn continuously along microscopic channels through its own nitridation product, thereby sustaining the growth process. Particles of AlN ranging in size from submicron to 20 μm can be observed. An interconnected AlN reaction product with an interconnected metal phase results in an AlN/Al matrix. The metallic phase is present as both interconnected tortuous channels and pockets. A TEM picture showing the AlN filler and the submicron AlN reaction product grains in the AlN/Al matrix is given in Fig. 1. The micrograph shows that the material has no appreciable porosity. By changing the beam direction with respect to the thin foil, a *spine-like* microstructure is observed in the AlN/Al matrix. As a consequence, strong strength anisotropy is expected at this microstructural level. Even if the filler phase disrupts the columnar structure, according to Nagelberg (1989) some preferred orientation of the reaction product seems to remain. Line and surface defects are observed in the AlN particles. In addition to low density dislocation defects, dome shaped defects are found in the AlN filler. These defects arise apparently from the presence of a low concentration of impurities (Hagege *et al.*, 1988).

3. EXPERIMENTAL METHOD AND RESULTS

3.1. *Normal impact experiments*

Normal impact experiments are performed to assess the Hugoniot elastic limit (HEL) of the material and its shear resistance under a state of uniaxial strain. The details of the experiments are given in Table 1. Two configurations are used in the experiments. In the *back surface configuration* a manganin gauge is embedded between the back surface of the AlN/AlN/Al composite plate and a thick PMMA plate. Since the mechanical impedances of the gauge substrate (glass epoxy) and PMMA are very similar, no stress reverberations are introduced at the gauge location and a sharp rise time is recorded. The elastic and plastic waves can be clearly identified in this configuration, as shown in the stress time profile plotted in Fig. 2. An HEL of 5.1 GPa was computed from the measured stress (σ_{m}) using the relation $\sigma_{\mathrm{HEL}} = \sigma_{\mathrm{m}}(Z_1 + Z_2)/2Z_2$, where $Z_1 = 30.4$ GPa mm^{-1} μs^{-1} is the impedance of the AlN/AlN/Al specimen and $Z_2 = 3.6$ GPa mm^{-1} μs^{-1} is the shock impedance of PMMA at $\sigma_{\mathrm{m}} = 1.08$ GPa. The calibrations of longitudinal manganin gauges under shock loading were taken from Rosenberg and Partom (1985). Based on the measured HEL, an unconfined initial dynamic yield strength (Y) can be computed if the von Mises yield condition is assumed. It can be shown that $Y = C_{\mathrm{s}}^2/C_{\mathrm{L}}^2\, \sigma_{\mathrm{HEL}} = 3.4$ GPa, in which C_{s} and C_{L} are the shear and longitudinal wave speeds.

A disadvantage of the back surface configuration is that the gauge records the stress transmitted to the PMMA and not the stress in the specimen. To accomplish stress measurement in the specimen, an *in-material gauge configuration*, in which a manganin gauge is sandwiched between two AlN/AlN/Al plates, has been used. In this case the gauge is fully encapsulated between the glass epoxy and mylar sheets to prevent gauge failure due to short circuiting. The recorded stress history is given in Fig. 3. The long rise time of the ramping wave, up to the break in the profile, is the result of the impedance mismatch between the specimen and the gauge package, and the existence of misalignment between the impactor and the target plates. The stress level at this break is approximately 6 GPa, which is higher than the value measured in the back surface configuration. This higher amplitude of the elastic precursor can be explained by its dependence on propagation distance (specimen thickness), which is typical of rate-dependent materials. As indicated in Table 1, sample thicknesses of 6.35 and 4.01 mm have been used. Another feature of the profile is the sudden interruption of the signal, at 500 ns, as a result of gauge failure. Short circuiting problems have been systematically encountered in experiments conducted on AlN polycrystalline ceramics by Rosenberg *et al.* (1991).

3.2. *Pressure-shear experiments*

Normal impact experiments, although valuable for providing direct means for assessing the validity of mathematical models of material response, contain two major limitations. First, for a large class of hard materials, the compressive wave profiles are controlled primarily by the elastic compressibility of the material and not by the material damage or plastic flow. Second, the imposed stress trajectories for loading and unloading correspond to a straight line in the space of components of the stress deviator tensor.

These two disadvantages can be overcome if the specimen is subjected to combined pressure-shear loading. Such loading is obtained by inclining the flyer and target to the axis of the projectile. A wide variety of non-proportional stress trajectories can be imposed by varying the angle of inclination. Limitations arise, particularly for ultra-hard materials, from sliding of the impact faces. As discussed in Espinosa and Clifton (1991), several pressure-shear configurations can be used in the study of brittle materials.

A symmetric pressure-shear configuration is obtained when the impactor and target plates are made of the material under study (see Fig. 4). In this case, the recorded wave profiles are determined by the inelastic response of the material through the thickness of the sample. Consequently, the wave profile is attenuated and spread, and the strain rates are decreased. All field variables are strong functions of position and time. A major disadvantage of this configuration is the possibility of spallation in the specimen under conditions of pure shear, region 2 in Fig. 4. It should be noted that loading conditions leading to high pressures and shearing rates are of primary interest in the characterization of advanced materials. In order to accomplish such loading, a modification to the symmetric pressure-shear configuration, in which a window interferometry is utilized, has been proposed by Espinosa and Clifton (1991).

The high strain rate pressure-shear configuration (Fig. 5a) offers some advantages over the symmetric impact configuration. In addition to achieving high pressures and shearing rates, this experiment allows the constitutive relation between stress, strain and strain rate to be obtained directly, provided the flyer and anvil plates remain elastic. Strain rates of the order of 10^5–10^6, and pressures between 5 and 12 GPa are obtained by impacting a thin specimen sandwiched between a hard flyer plate and a hard anvil plate. If the flyer and anvil remain elastic, stresses, shear strains and strain rates can be obtained by measuring the impact velocity and the transverse particle velocity at the rear surface of the anvil plate.

In the characterization of hard ceramics and composites, very demanding requirements are placed on the flyer and anvil plates. These plates must be hard enough in compression and shear to remain elastic at the high stress levels required for the inelastic deformation of the specimen, yet strong enough in tension to prevent failure at 45° when the shear wave propagates through the unloaded region adjacent to the rear surface of the anvil. Appropriate flyer and anvil materials that remain elastic during the wave propagation event are very difficult to find in the case of strong ceramics and ceramic composites. Therefore, it becomes necessary to perform numerical simulations of the experiment for the proper identification of inelastic mechanisms responsible for the material behavior. It should be noted that the departure from this ideal condition may be small enough, as in the present investigation, to allow for the material characterization under pressures and strain rates that otherwise cannot be obtained.

The experimental results for the case in which a thin AlN/AlN/Al composite specimen is sandwiched between two WC/6Co plates are described next. The normal velocity–time profile corresponding to this experiment is shown in Fig. 5b. The reduction in particle velocity after the initial jump indicates the presence of a small gap at the AlN/AlN/AlWC/6Co interface in the flyer assembly. While this gap can be completely eliminated for soft metal specimens by means of diffusion bonding (Tong, 1991), the scenario is much more complicated for the case of hard materials. The velocity rise upon the closure of the gap is associated with the reverberation of waves within the specimen. This part of the data corresponds to a non-homogeneous deformation state and cannot be used directly for the characterization of the material properties. The normal particle velocity rises ultimately to the value predicted by the symmetric impact of WC/6Co.
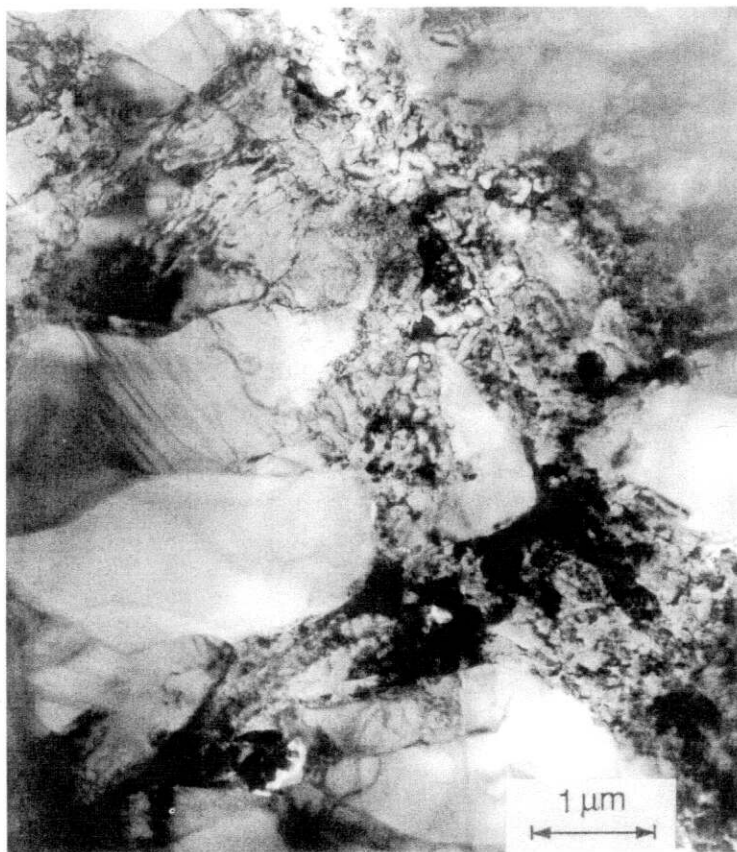
Fig. 1. TEM bright field image showing the AlN filler particles and the AlN/Al matrix.

Table 1. Summary of experiments

Shot no.	Projectile velocity [V_0 (mm μs^{-1})]	Skew angle [α (degrees)]	Specimen thickness [h (mm)]	Impactor	Back plate
91-05	0.1507	26.6	0.294	WC/6Co	WC/6Co
91-09	0.197	18	5.94	WC/6Co	WC/6Co
92-01	0.422	0	4.01	WC/6Co	AlN/AlN/Al
93-01	0.580	0	6.35	Cu	PMMA
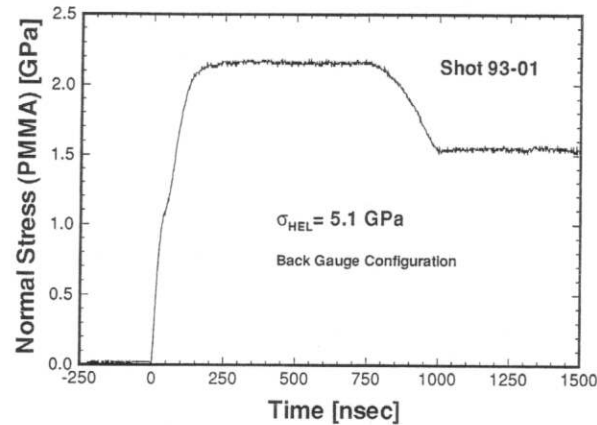
Fig. 2. Normal stress at the AlN/AlN/Al-PMMA interface in back surface configuration.
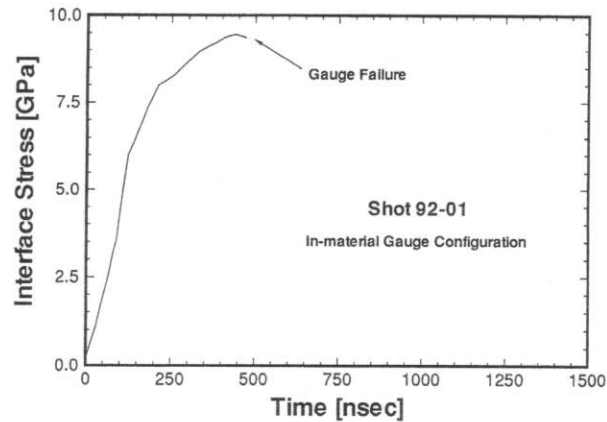
Fig. 3. Stress profile corresponding to the in-material gauge configuration.

The transverse particle velocity, given in Fig. 5c, follows a history similar to that observed for the normal stress during the initial 200 ns. Thus, the frictional behavior at the impact surfaces seems to control the shear response during this period of time. After the sudden drop in transverse velocity, the shear stress rises to a maximum value followed by a slowly decreasing slope in the next 1.5 μs. A shear stress of approximately 0.8 GPa is measured, which corresponds to an unconfined post yield dynamic strength $Y = 2\tau = 1.6$ GPa. Comparison of this result with the initial dynamic yield strength computed in Section 3.1, clearly indicates a dramatic material softening with accumulated inelastic deformation. Some peaks and valleys in the transverse velocity history are observed, which appear too large to be attributed to the data reduction process. Similar features have been observed in the transverse velocity histories measured in symmetric pressure-shear experiments performed on SiC by Klopp and Shockey (1991). They may be explained by a sequence of sliding-sticking conditions or by the development of heterogeneous damage within the sample. The first possibility appears to be less likely in view of the sustained shear stress
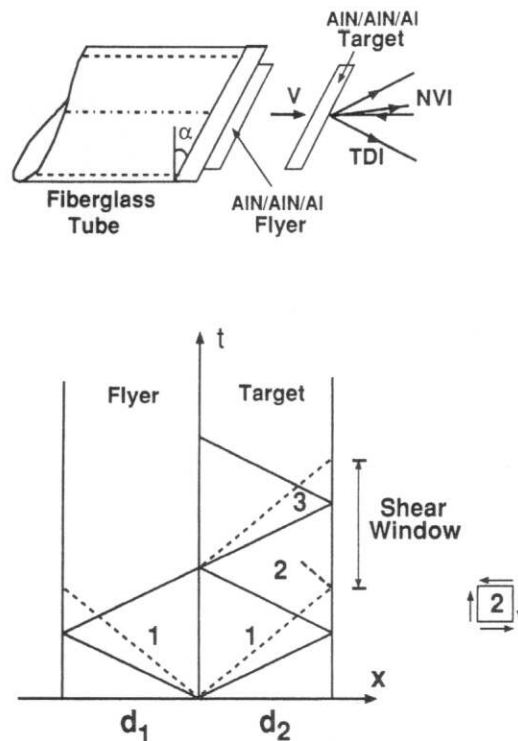
Fig. 4. Schematic of symmetric pressure-shear configuration; lagrangian t–X diagram.

upon arrival of the longitudinal unloading wave at the specimen–anvil interface at approximately 1.2 μs.

4. MODELING

4.1. A microcracking multiple-plane model

In this section the inelastic response of brittle and quasi-brittle materials is modeled through a microcracking multiple-plane model based on a dilute approximation (Taylor model). Our formulation overlaps with some theories in which multiple-plane representations of inelasticity are derived [e.g. Seaman and Dein (1983), Bazant and Gambarova (1984), Ju and Lee (1991)]. In the quasistatic case, Ju and Lee (1991), employed a self-consistent method together with an analytical solution for weakly interacting cracks in order to derive inelastic compliances. Unfortunately, the averaging methods used to compute effective moduli do not admit a straightforward extension into the dynamic range.

The basic concept is that microcracking and/or slip can occur on a discrete number of orientations (Fig. 6). In our computational model, the slip plane properties (friction, initial microcrack size, microcrack density, etc.) and their evolution are *independently* computed on each plane. The macroscopic response of the material is based on an additive decomposition of the strain tensor into an elastic part and an inelastic contribution arising from the presence of microcracks within the solid. In contrast to scalar representations of damage [e.g. Rajendran (1992)] the present formulation is broad enough to allow the examination of damage induced anisotropy and damage localization in the interpretation of plate impact experiments.

4.1.1. *Stress-strain relations in tension.* Consider a representative volume V of an elastic solid containing a large number of microcracks. The average strains contributed by the open microcracks are given by
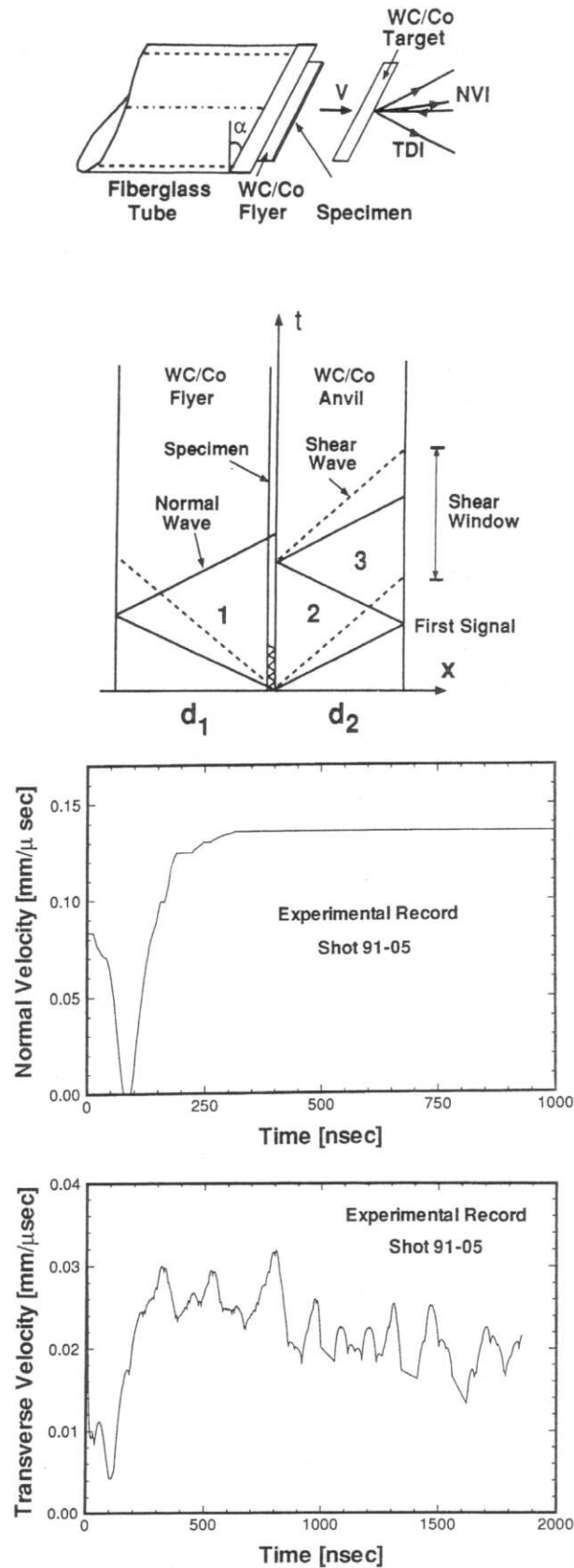
Fig. 5. (a) Schematic of high strain rate pressure-shear configuration; lagrangian *t–X* diagram. (b) Normal velocity history at the free surface of the anvil plate. (c) Transverse velocity history at the free surface of the anvil plate.
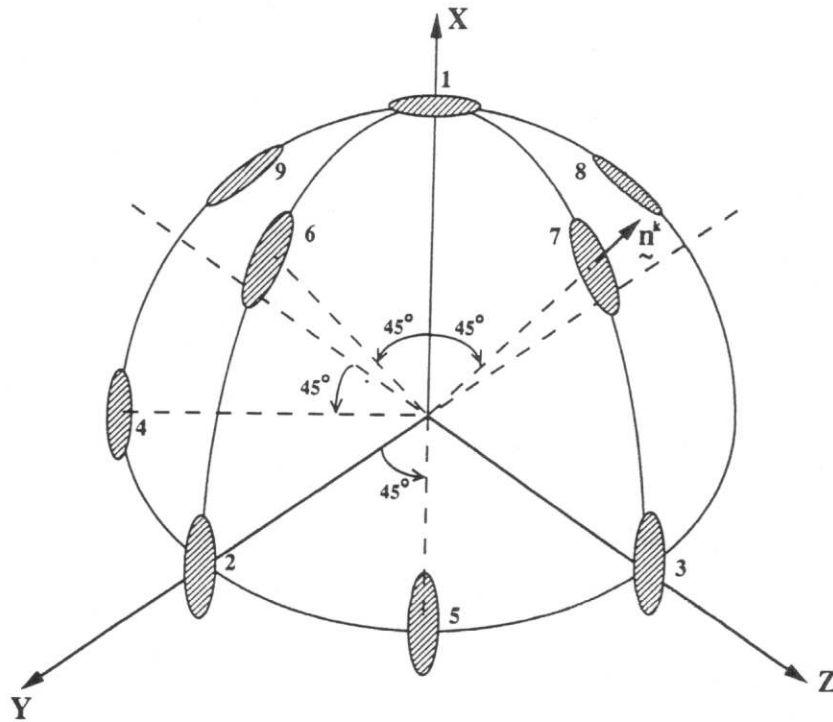
Fig. 6. Schematic of microcracking multiple-plane model.

$$\varepsilon_{ij}^{c} = \frac{1}{V} \sum_{k} \int_{S^{(k)}} \tfrac{1}{2} (b_{i}^{(k)} n_{j}^{(k)} + n_{i}^{(k)} b_{j}^{(k)}) \, \mathrm{d}S, \tag{1}$$

where the subindex k is used to label the microcracks, with $S^{(k)}$ denoting the surface of microcrack k, $\mathbf{n}^{(k)}$ the corresponding unit normal, and $\mathbf{b}^{(k)}$ the displacement jump across $S^{(k)}$. Here we consider loading conditions leading to crack opening, i.e. the displacement jumps $\mathbf{b}^{(k)}$ have a positive component in the normal direction $\mathbf{n}^{(k)}$, namely,

$$b_{i}^{(k)} n_{i}^{(k)} \geqslant 0. \tag{2}$$

Let $\boldsymbol{\sigma}$ denote the applied stress field which would be present in the representative volume where the solid is uncracked. For a penny crack of radius a in an infinite isotropic elastic solid subjected to remote uniform stress $\boldsymbol{\sigma}$, the expression for $\mathbf{b}$ is given by Willis (1968) as

$$b_{i} = \frac{8(1-v^{2})}{\pi E(2-v)} \sqrt{a^{2}-r^{2}} [2\sigma_{ij} n_{j} - v\sigma_{jk} n_{j} n_{k} n_{i}], \tag{3}$$

where E and v are the Young's modulus and Poisson's ratio of the uncracked solid (matrix), respectively, and r denotes the distance to the center of the microcrack. Assume now that the applied stresses can be taken to be nearly uniform over each microcrack. Following Kachanov (1980) we note that, if the density of microcracks is low enough that their interaction can be neglected, and all microcracks are assumed to be planar, then

$$\varepsilon_{ij}^{c} = \frac{1}{V} \sum_{k} S^{(k)} \tfrac{1}{2} (\bar{b}_{i}^{(k)} n_{j}^{(k)} + n_{i}^{(k)} \bar{b}_{j}^{(k)}), \tag{4}$$

where

$$\bar{b}_i^{(k)} = \frac{1}{S^{(k)}} \int_{S^{(k)}} b_i^{(k)} \, dS = \frac{16(1-v^2)}{3E(2-v)} a^{(k)} (2\sigma_{ij} n_j^{(k)} - v\sigma_{jl} n_j^{(k)} n_l^{(k)} n_i^{(k)}) \tag{5}$$

is the average displacement jump across microcrack k.

Within the framework of a multiple-plane model with nine independent orientations of microcracks (see Fig. 6), the inelastic strain tensor is given by

$$\varepsilon_{ij}^c = \sum_{k=1}^{9} N^{(k)} S^{(k)} \frac{1}{2} (\bar{b}_i^{(k)} n_j^{(k)} + n_i^{(k)} \bar{b}_j^{(k)}) \tag{6}$$

in which $N^{(k)}$ is the microcrack density of each orientation. In the present formulation, $N^{(k)}$ is assumed constant, although an initial distribution as a function of stress and an evolution equation could be proposed (Seaman et al., 1978). At the present time, information on $N^{(k)}$ and its evolution are not available for the material under investigation. Development of recovery experiments, which will allow the post test examination of the samples, is needed.

4.1.2. *Stress–strain relations in compression.* The point of departure is again eqn (6) which gives the average inelastic strain, due to microcracking, of a representative volume of material. Because the inequality (2) is not satisfied in this case, the effective shear traction can be defined as

$$f_i = (\tau + \mu\sigma_n)(\mathbf{n}_\tau)_i, \tag{7}$$

in which μ is the friction coefficient of the microcrack faces, τ and σ_n are the resolved shear stress and the normal stress acting on the microcrack, respectively, and $\mathbf{n}_\tau$ is the unit vector in the direction of the resolved shear traction. Throughout this section the superindex k is implicit.

The average sliding of the faces of the crack, following from Willis' result (3), is

$$\bar{b}_i = \frac{32(1-v^2)}{3\pi E(2-v)} a f_i. \tag{8}$$

Embodied in eqn (8) is the notion that $\mathbf{f}$ provides the effective driving force for the sliding of the microcracks. A revealing alternative form of eqn (8) may be derived as follows. Let $\bar{b} = |\bar{\mathbf{b}}|$ be the magnitude of the sliding displacement. Then, multiplying eqn (8) by $\mathbf{t}$ and after some rearrangement, one finds that the relation

$$\phi(\sigma_n, \tau, \bar{b}) \equiv \tau + \mu\sigma_n - \frac{3\pi E(2-v)}{32(1-v^2)a} \bar{b} = 0 \tag{9}$$

must be identically satisfied during sliding. Equation (9) may be regarded as a balance of forces: the first term τ represents the externally applied driving force; the second, $\mu\sigma_n$, the frictional resistance; and the third, the restoring force from the surrounding elastic medium. When sliding occurs, the friction condition (9) together with the equation of evolution for a determine the evolution of $\bar{b}$.

4.1.3. *Dynamic microcrack growth.* In order to compute the inelastic strain tensor at all times, it becomes necessary to follow the evolution of the microcrack radius $a(\mathbf{n})$ in the selected orientations. The structure of this equation is obtained by means of the following argument. Assume that microcrack growth is governed by a dynamic toughness, $K_d(\dot{a})$, which depends on the crack tip velocity, i.e. growth is sustained provided that

$$K(a, \dot{a}; t) = K_d(\dot{a}), \tag{10}$$

where K is an effective dynamic stress intensity factor on the microcrack front. For a given loading, K may be expected to be a function of the current crack size a, the velocity of the crack tip $\dot{a}$, and the time t, through the temporal dependence of the loading. Under rather general circumstances, it may be shown (Freund, 1990) that K has the multiplicative structure

$$K(a, \dot{a}; t) = k(\dot{a})K(a, 0; t), \tag{11}$$

where $k(\dot{a})$ is a universal function of $\dot{a}$ and $K(a, 0; t)$ is the stress intensity factor which would have resulted had the crack always been at the instantaneous position represented by a. The function k takes the value of 1 for $\dot{a} = 0$ and tends to zero for $\dot{a}$ approaching the Rayleigh wave speed c_R in Mode I, and the shear wave speed c_2 in Mode II. In the few problems for which closed form analytical solutions exist (Broberg, 1978; Freund, 1972a,b, 1990), k is well approximated by a function of the type

$$k(\dot{a}) \approx (1 - \dot{a}/c)^{\alpha}, \tag{12}$$

where c is the appropriate choice of wave speed and α is approximately 1.

To complete the definition of the crack tip equation of motion, $K(a, 0, t)$ must be related to the applied stress history. First, we consider the case of tensile principal stresses. Here we consider isolated penny-shaped cracks subjected to normal stress σ_n. For definiteness, imagine that the microcracks are subjected to a step tensile pulse of amplitude σ^*. Then, the stress intensity factor grows initially as $\sqrt{t}$ (Freund, 1990), so that an incubation time t_i, is required before the crack growth initiation toughness K_{IC} is attained. This incubation time is of the order $t_i \sim K_{IC}^2/(\sigma^*)^2 c_1$. Taking as representative of the conditions of the test $\sigma^* \sim 600$ MPa, $K_{IC} \sim 2$MPa$\sqrt{m}$, and $c_1 \sim 6.4$ mm μs^{-1}, the incubation time is estimated to be of the order $t_i \sim 1.7$ ns. This is much shorter than any of the transient times characteristic of the loading, and thus incubation times may be safely neglected. For the stationary crack, the applied stress pulse gives rise to a complex transient in the stress intensity factor, which has oscillations of diminishing amplitude about the asymptotic limit (Freund, 1990; Sneddon, 1946)

$$K(a, 0; \infty) = 2\sigma^* \sqrt{a/\pi}. \tag{13}$$

Numerical solutions (Chen and Wilkins, 1976; Chen and Sih, 1977) suggest that this limit is quite closely realized after times of the order of a few multiples of $t_c = a/c_1$. Taking $a \sim 10 \ \mu$m as a representative value, one obtains $t_c \sim 1.6$ ns, which is again negligible under the conditions of the specimen. Thus, for the purposes of the present analysis the stress intensity factor transients may be neglected and $K(a, 0; t)$ can be taken directly as

$$K(a, 0; t) = 2\sigma_n(t)\sqrt{a(t)/\pi}. \tag{14}$$

Finally, the dependence of the dynamic toughness K_d on crack tip velocity needs to be considered. As noted earlier, microscopy observations on the AlN/AlN/Al clearly indicate that microcrack growth can be accompanied by substantial plastic flow. Under similar conditions in metals, K_d is known to be a monotonically increasing function of $\dot{a}$. Furthermore, analysis by Freund and Hutchinson (1985) indicates that K_d should become unbounded as $\dot{a}$ approaches the Rayleigh wave speed c_R. A simple form of K_d consistent with these requirements is

$$K_d(\dot{a}) = K_{IC}/(1-\dot{a}/c_R)^\beta, \tag{15}$$

where K_{IC} is the initiation toughness and β a phenomenological material constant. Combining eqns (11), (12), (14) and (15), we arrive at the following crack tip equation of motion

$$\dot{a} = c_R[1-(K_{IC}/2\sigma_n\sqrt{a/\pi})^m] \geqslant 0, \tag{16}$$

where $m = 1/(\alpha+\beta)$. The inequality in (16) restricts $\dot{a}$ to be positive, i.e. the crack remains stationary if the right-hand side of (16) is negative.

The extension of the above formulation to the case of mixed mode loading is straightforward. In this case the evolution equation for $\dot{a}$ is

$$\dot{a} = nc_R[1-(K_{IC}/K_{eff})^m] \geqslant 0, \tag{17}$$

where n and m are phenomenological material constants which may have different values in tension and compression, and K_{eff} is an effective stress intensity factor. For mixed mode conditions, K_{eff} is derived by considering an average energy release rate associated with an increase in radius of the microcracks, namely,

$$\mathscr{G} = \frac{1}{2\pi}\int_0^{2\pi} \frac{1-v^2}{E}[K_I^2 + K_{II}^2 + K_{III}^2/(1-v)]\,d\theta \tag{18}$$

and,

$$K_{eff} = \sqrt{\frac{\mathscr{G}E}{1-v^2}}. \tag{19}$$

The crack tip equation of motion (17) has previously been used in the high strain rate modeling of Al_2O_3 by Clifton et al. (1992), Espinosa, (1989, 1992), and Rajendran (1992).

4.1.4. *Numerical implementation.* The general structure of the constitutive equations corresponds to that of a viscoplastic solid with elastic degradation. In particular, the effective behavior of the solid is predicted to be rate dependent. From a computational standpoint, this ensures numerical reliability and mesh independence (Needleman, 1988). This is in contrast to quasistatic formulations of damage for which the governing equations become ill-posed in the softening regime (Sandler and Wright, 1984).

Based on an additive decomposition of the strain tensor, and assuming Hooke's law, the equations governing the response of the material are

$$\sum_{k=1}^9 \frac{1}{2}N^k S^k(\bar{\mathbf{b}}^k\mathbf{n}^k + \mathbf{n}^k\bar{\mathbf{b}}^k) = \varepsilon - \left(\frac{1+v}{E}\sigma - \frac{v}{E}\sigma_{kk}\mathbf{I}\right). \tag{20}$$

The expression for $\mathbf{b}^k$ is a function of the loading mode on each plane as previously discussed. For simplicity, only the equations corresponding to the compressive mode will be given in detail. A similar treatment applies to the other cases.

Substitution of eqn (8) into eqn (20) gives the following stress-strain relations:

$$\sum_{k=1}^9 \frac{16(1-v^2)}{3E(2-v)}(a^k)^3 N^k[(\sigma\cdot\mathbf{n}^k)\mathbf{n}^k + \mathbf{n}^k(\sigma\cdot\mathbf{n}^k) - (\mathbf{n}^k\cdot\sigma\cdot\mathbf{n}^k)(2\mathbf{n}^k\mathbf{n}^k - \mu(\mathbf{n}_\tau)^k\mathbf{n}^k - \mu\mathbf{n}^k(\mathbf{n}_\tau)^k)]$$

$$= \varepsilon - \left[\frac{1+v}{E}\sigma - \frac{v}{E}\sigma_{kk}\mathbf{I}\right]. \tag{21}$$

Differentiation of eqn (21) with respect to time provides the constitutive equations in rate form. Fully implicit integration of this equation is computationally too intensive, while explicit integration lacks accuracy and becomes unstable during unloading when substantial damage within the material has developed. These disadvantages were overcome through the use of a semi-implicit scheme in which the crack-tip equation of motion, and the direction of the shear traction on the microcrack plane are explicitly updated, while the remaining variables are treated implicitly. Under these conditions, the relation between the stress rate tensor and the total strain rate tensor becomes

$$\left(\frac{1+v}{E}\dot{\boldsymbol{\sigma}} - \frac{v}{E}\dot{\sigma}_{kk}\mathbf{I}\right) + \sum_{k=1}^{9}\frac{16(1-v^2)}{3E(2-v)}N^k((a^k)^3 + 3(a^k)^2\dot{a}^k\Delta t)[(\dot{\boldsymbol{\sigma}}\cdot\mathbf{n}^k)\mathbf{n}^k + \mathbf{n}^k(\dot{\boldsymbol{\sigma}}\cdot\mathbf{n}^k)$$

$$- (\mathbf{n}^k\cdot\dot{\boldsymbol{\sigma}}\cdot\mathbf{n}^k)(2\mathbf{n}^k\mathbf{n}^k - \mu(\mathbf{n}_\tau)^k\mathbf{n}^k - \mu\mathbf{n}^k(\mathbf{n}_\tau)^k]_{i+1}$$

$$+ \sum_{k=1}^{9}\frac{16(1-v^2)}{3E(2-v)}N^k(a^k)^3\mu(\mathbf{n}^k\cdot\dot{\boldsymbol{\sigma}}\cdot\mathbf{n}^k)_{i+1}[(\mathbf{n}^k\dot{\mathbf{n}}_\tau^k + \dot{\mathbf{n}}_\tau^k\mathbf{n}^k)]\Delta t$$

$$= \dot{\boldsymbol{\varepsilon}}_{i+1} - \sum_{k=1}^{9}\frac{16(1-v^2)}{3E(2-v)}N^k 3(a^k)^2\dot{a}^k[(\boldsymbol{\sigma}\cdot\mathbf{n}^k)\mathbf{n}^k + \mathbf{n}^k(\boldsymbol{\sigma}\cdot\mathbf{n}^k) - (\mathbf{n}^k\cdot\boldsymbol{\sigma}\cdot\mathbf{n}^k)(2\mathbf{n}^k\mathbf{n}^k$$

$$- \mu(\mathbf{n}_\tau)^k\mathbf{n}^k - \mu\mathbf{n}^k(\mathbf{n}_\tau)^k]_i - \sum_{k=1}^{9}\frac{16(1-v^2)}{3E(2-v)}N^k(a^k)^3\mu(\mathbf{n}^k\cdot\boldsymbol{\sigma}\cdot\mathbf{n}^k)_i[(\mathbf{n}^k\dot{\mathbf{n}}_\tau^k + \dot{\mathbf{n}}_\tau^k\mathbf{n}^k)], \qquad (22)$$

in which the indices i and $i+1$ refer to two subsequent times. This equation corresponds to the case in which the effective shear traction on the surface of the crack is such that additional slipping occurs, i.e. $\dot{\mathbf{b}}^k > 0$. Similar expressions can be derived for the sticking case, in which eqn (9) is satisfied with $\dot{\mathbf{b}}^k = 0$. Equation (22) can be written in matrix form and the stress rate tensor obtained by simple elimination. After the stress rate tensor is known, the average displacement jump rates and inelastic strain rates can be computed from the following equations:

$$\dot{\bar{\mathbf{b}}}^k = \frac{32(1-v^2)}{3\pi E(2-v)}[a^k(|\dot{\tau}|^k + \mu\dot{\sigma}_n^k)\mathbf{n}_\tau^k + \dot{a}^k(|\tau|^k + \mu\sigma_n^k)\mathbf{n}_\tau^k + a^k(|\tau|^k + \mu\sigma_n^k)\dot{\mathbf{n}}_\tau^k], \qquad (23)$$

$$\dot{\boldsymbol{\varepsilon}}^c = \sum_{k=1}^{9}N^k\left[\pi a^k\dot{a}^k(\bar{\mathbf{b}}^k\mathbf{n}^k + \mathbf{n}^k\bar{\mathbf{b}}^k) + \frac{S^k}{2}(\dot{\bar{\mathbf{b}}}^k\mathbf{n}^k + \mathbf{n}^k\dot{\bar{\mathbf{b}}}^k)\right]. \qquad (24)$$

4.2. A pressure dependent viscoplastic model

Pressure-shear experiments conducted on the AlN/AlN/Al composite (Espinosa and Clifton, 1991) reveal the material possesses a strong pressure-sensitive inelastic behavior. From the previous description of the microstructure and the TEM micrographs showing the AlN filler particles surrounded by a matrix composed of submicron grains of AlN reaction product and Al alloy, the origin of this pressure sensitivity appears to be in the kinematics of the deformation process. For the material to sustain finite deformations in shear, the hard AlN filler particles have to rotate and translate relative to each other with plastic deformation. Furthermore, microcracking of the AlN reaction product present in the AlN/Al matrix is then necessary, which leads to strain softening of the composite. By considering the obstacles that each filler particle has to overcome in its relative motion, it may be possible to rationalize the importance of the normal stress. Consequently, as an alternative inelastic mechanism, a pressure dependent plastic flow with strain softening is considered next. The plastic flow in the composite material is defined by a pressure dependent Drucker and Prager yield criterion given by

$$F = q + \alpha(p - p_0) = 0 \tag{25}$$

in which q is the effective stress, and p is the pressure. Note that the yield surface in (p, q)-space has a corner at $p = p_0$. The cone of attraction of the vertex is the region $q/3\mu \leqslant (p - p_0)/\beta k$. A non-associated flow rule is employed to account for dilatancy (Leroy and Ortiz, 1988). The expressions for the flow potential are

$$G = q + \beta(p - p_0) \quad \text{if} \quad q/3\mu \geqslant (p - p_0)/\beta k,$$

$$G = \sqrt{3\mu + \beta^2 k} \sqrt{q^2/3\mu + (p - p_0)^2/k} \quad \text{otherwise} \tag{26}$$

where μ is the shear modulus, k is the bulk modulus, and α and β are related to the friction and dilatancy angles ϕ and ψ, respectively, as

$$\alpha = \frac{6 \sin \phi}{3 - \sin \phi}, \quad \beta = \frac{6 \sin \psi}{3 - \sin \psi}. \tag{27}$$

The plastic strain rates are given by:

$$\dot{\varepsilon}_{ij}^{\text{p}} = \dot{\varepsilon}^{\text{p}} \, \partial G/\partial \sigma_{ij}, \tag{28}$$

where $\dot{\varepsilon}^{\text{p}}$ is an effective plastic strain.

An elliptical transition of α between an initial and a saturation friction coefficient, α_0 and α_{sat} respectively, is utilized to describe material hardening and softening. If $\alpha_0 < \alpha_{\text{sat}}$, the material hardens; softens if $\alpha_0 > \alpha_{\text{sat}}$ and becomes ideally plastic for $\alpha_0 = \alpha_{\text{sat}}$. The evolution of α is defined by the following functional dependence on the effective plastic strain

$$\alpha(\varepsilon^{\text{p}}) := \alpha_0 + (\alpha_{\text{sat}} - \alpha_0) \sqrt{1 - (\varepsilon^{\text{p}} - \varepsilon_{\text{sat}}^{\text{p}})^2/\varepsilon_{\text{sat}}^{\text{p}}{}^2},$$

$$\alpha(\varepsilon^{\text{p}}) = \alpha_{\text{sat}} \quad \text{if} \quad \varepsilon^{\text{p}} \geqslant \varepsilon_{\text{sat}}^{\text{p}}. \tag{29}$$

An extended Duvaut–Lions viscoplasticity model (Simo et al., 1988; Ju, 1992) is used to introduce rate dependence in the above plasticity model. In this model the viscoplastic strain rate is given by

$$\varepsilon_{ij}^{\text{vp}} = C_{ijkl}^{\text{e}} \frac{\sigma_{kl} - P_{kl}(\boldsymbol{\sigma})}{T_{\text{R}}} \quad \text{if} \quad F(p, q, \mathbf{v}) > 0, \tag{30}$$

in which P is the closest-point projection in the metric induced by the elasticity tensor C^{-1} onto the yield surface; and T_{R} is a viscosity coefficient that plays the role of a relaxation time. The internal variable vector $\mathbf{v}$ is defined as

$$\dot{\mathbf{v}} = \frac{-(\mathbf{v} - \bar{\mathbf{v}})}{T_{\text{R}}}, \tag{31}$$

where $\bar{\mathbf{v}}$ is the inviscid solution of the rate-independent elastoplastic problem.

A backward-Euler algorithm, which is unconditionally stable with respect to the time increment (Ortiz and Popov, 1985), is employed in the calculations.

5. NUMERICAL SIMULATIONS

Stress and velocity histories obtained by simulation of the normal and pressure-shear experiments, with the modified Drucker–Prager model incorporating softening, pressure and rate dependence, and the microcracking multiple-plane model are discussed next. In
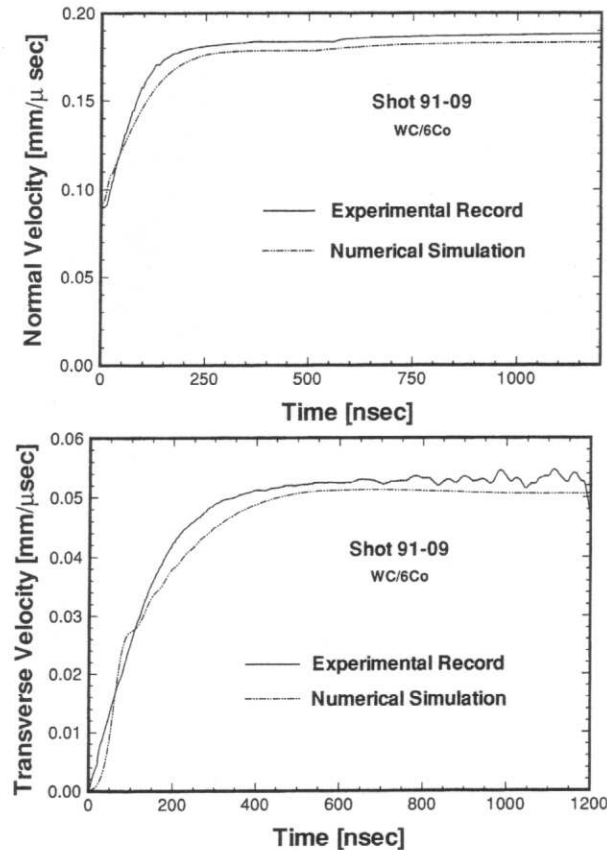
H. D. Espinosa

Fig. 7. (a) Normal velocity history obtained by symmetric pressure-shear impact of WC/6Co plates. Comparison between experimental record and numerical simulation. (b) Transverse velocity history obtained by symmetric pressure-shear impact of WC/6Co plates. Comparison between experimental record and numerical simulation.

the simulations of the pressure-shear experiment, the existence of a gap at the flyer–specimen interface has been incorporated in the simulation. Furthermore, a pressure-dependent plasticity model has been used in the material description of the WC/6Co plates. The model parameters have been selected to reproduce results obtained in an earlier investigation (Espinosa, 1992) in which a symmetric pressure-shear impact experiment was conducted. The history of normal and shear velocities at the back surface of the specimen are given in Fig. 7a and b, respectively. Both velocity histories clearly indicate the inelastic behavior of the material at this level of normal and shear stresses. The results from the numerical simulation are also shown in the same figures. Although, additional experiments are necessary for a full description of the WC/6Co mechanical behavior under dynamic loading, the present model is considered appropriate for the loading conditions to which the material is subjected in the reported pressure-shear experiments.

The computed stress histories obtained in the simulation of the normal impact experiment, using the in-material gauge configuration, are shown in Fig. 8. As discussed in Section 3.1, in the in-material gauge configuration the elastic precursor is not well defined due primarily to wave reverberations at the gauge location. Consequently, direct comparison between the numerical simulations and the experimental record at the precursor arrival is not possible without a proper simulation of the gauge package geometry and impedance. Nonetheless, when the stress profile measured in the back surface configuration is considered, one concludes that the stress history predicted by the modified Drucker–Prager model, with the parameters defined in Table 2 (set 2), reproduces the main features observed experimentally. If another set of parameters is used in the material modeling, Table 2 (set 1), i.e. a lower inelastic threshold and a smaller rate sensitivity, the predicted elastic precursor is well below the HEL of the material. Furthermore, a typical separation
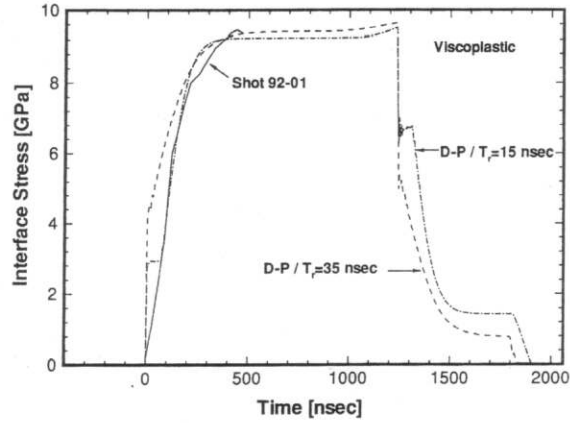
Fig. 8. Interface stress histories obtained by numerical simulation of normal impact experiment with an elasto-viscoplastic model. Effect of model parameters on elastic precursor and wave structure.

Table 2. Parameters used in the numerical simulations with the elasto-viscoplastic model

Model parameters	Set 1	Set 2
p_0	7 GPa	7 GPa
ϕ_0	6°	8°
ψ	0°	0°
ϕ_{sat}	1.5°	4°
ε_{sat}^p	0.1	0.1
T_R	15 ns	35 ns
E	250 GPa	250 GPa
v	0.25	0.25

between the elastic and inelastic waves occurs resulting in the formation of a step at the stress level corresponding to the HEL. This feature is not observed in the stress history recorded experimentally (Fig. 2), implying that the material has indeed a rate dependent behavior. Lack of separation between the elastic and inelastic waves has also been observed in many ceramics like Al_2O_3, AlN, and SiC (Kipp and Grady, 1989; Rosenberg et al., 1991).

When the modified Drucker–Prager model is used in the simulation of the pressure-shear experiments with the parameters shown in Table 2 (set 2), the shear resistance of the material is over-predicted (see Fig. 9). In the same figure, the velocity history corresponding to a lower inelastic threshold and rate dependence, Table 2 (set 1), is shown. In this case
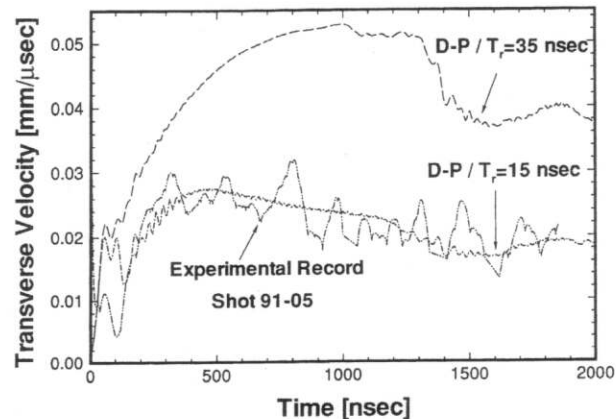

Fig. 9. Transverse velocity histories obtained by numerical simulation of high strain rate pressure-shear experiment with an elasto-viscoplastic model. Comparison with experimental record from shot 91-05.
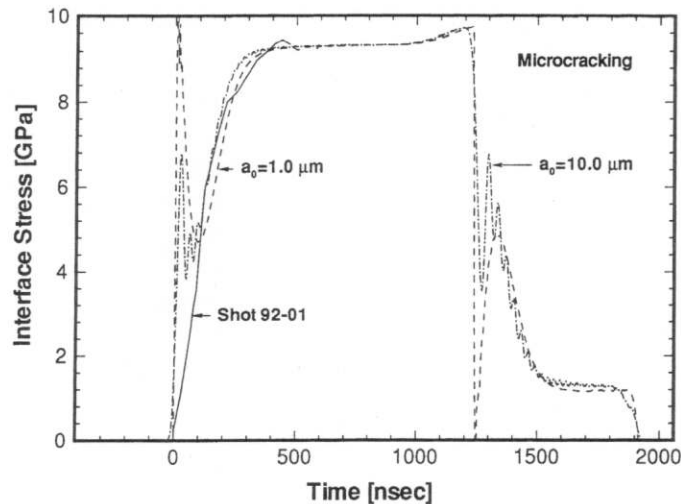
H. D. Espinosa

Fig. 10. Interface stress histories obtained by numerical simulation of normal impact experiment with a microcracking multiple-plane model.

overall agreement is obtained including a continuous reduction in transverse particle velocity resulting from strain softening. A further reduction in shear velocity, at approximately 1.2 μs, results from a progressive pressure release, at the impact surface, upon arrival of the normal unloading wave generated at the back surface of the anvil plate. The progressive pressure reduction is primarily due to the rise time associated with longitudinal wave reverberation in the specimen, both during the initial loading and unloading, and the inelastic behavior of the anvil plate.

In order to gain additional insight about the material shear resistance as a function of the impact configuration, and the inadequacy of the continuum elasto-viscoplastic model in reproducing both normal and pressure-shear experimental records with a single set of parameters, simulations of the experiments were performed utilizing the microcracking multiple-plane model described in Section 4. Guided by SEM and TEM microscopy studies conducted on the AlN/AlN/Al composite, in which no microcracks were observed, a small initial crack radius, $a_0 = 1.0$ μm, was selected. A crack density, $N = 1. \times 10^{13}$, was used on all nine orientations. This density is consistent with the number of interfaces per unit volume that can be computed, based on the measured average grain size of the AlN particles and AlN/Al matrix. The remaining parameters used in the simulations were: $\mu = 0.15$, $n^+ = n^- = 0.1$, $K_{IC} = 0.5$ MPa$\sqrt{m}$, and $m^+ = m^- = 0.3$. It should be noted that the value of K_{IC} used in the micromechanical model corresponds to the fracture toughness of the ceramic/ceramic interfaces. Its value is smaller than the macroscopic K_{IC} reported in Section 2 which includes crack kinking, bridging and friction.

In Fig. 10 normal stress profiles obtained with this model, at the gauge location, are shown. When an initial crack radius of 1 μm is used, absence of stress attenuation at the wave front seems to result from a small initial inelastic strain rate. By contrast, some attenuation occurs when the initial crack radius is increased to 10 μm due to frictional sliding along microcracks planes, which leads to a significant initial inelastic strain rate. Based on these elastic precursor observations, one can infer that ductile flow of the AlN/Al matrix, and not microcracking, seems to be the dominant source of inelasticity at the initial stages of inelasticity. A strong stress attenuation is observed behind the wave front as a result of dynamic crack growth on orientations 4, 5, 6, 8, followed by an upward slope until a plateau develops at a stress level of approximately 9.5 GPa. The microcrack radius evolutions on the nine independent orientations, at the impact and back surfaces of the specimen, are given in Fig. 11. Under the applied compressive field, the only active orientations are those at which the shear traction is maximum, mainly, orientations at 45° with respect to the impact direction (y–y in Fig. 6).

The velocity histories at the back surface of the anvil plate, obtained by simulation of the high strain rate pressure-shear experiment described in Section 3.2, are given in Fig. 12.
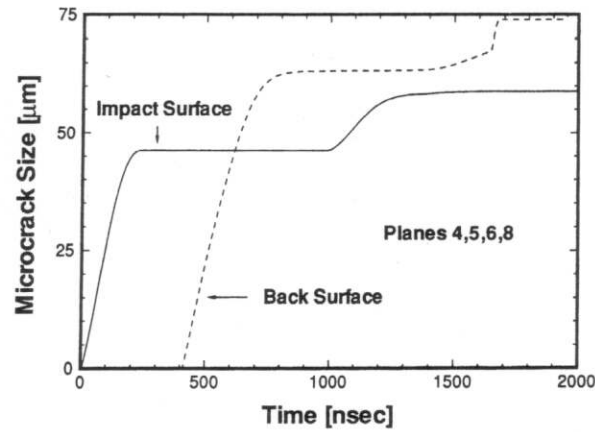
Fig. 11. History of microcrack sizes in normal impact experiment at two locations within the specimen.
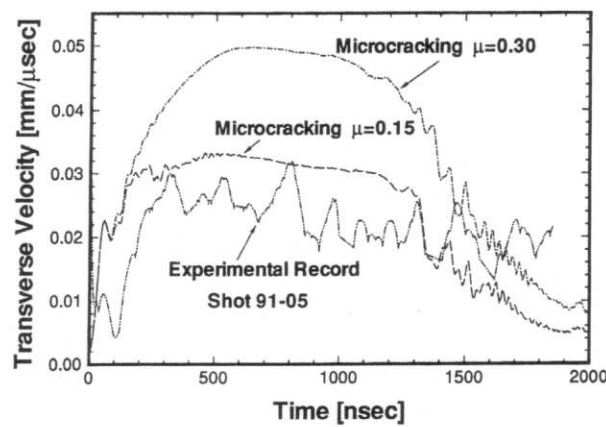

Fig. 12. Transverse velocity histories obtained by numerical simulation of high strain rate pressure-shear experiment with a microcracking multiple-plane model. Comparison with experimental record from shot 91-05.

The multiple-plane microcracking model with the set of parameters previously defined is utilized. In the numerical simulation, the normal motion is applied along the y–y direction, and the shear motion is applied along the x–x direction (see Fig. 6). The microcracking model predicts reasonably well the shear flow of the material as well as the progressive reduction in transverse particle velocity due to softening. The microcrack radius evolutions on the nine independent orientations are given in Fig. 13. It is observed that during the first
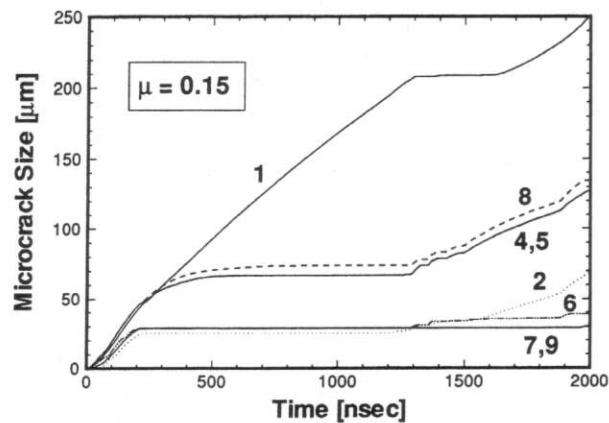

Fig. 13. History of microcrack sizes in high strain rate pressure-shear experiment. Note that only plane 1 has a continuously growing microcrack radius until unloading occurs.
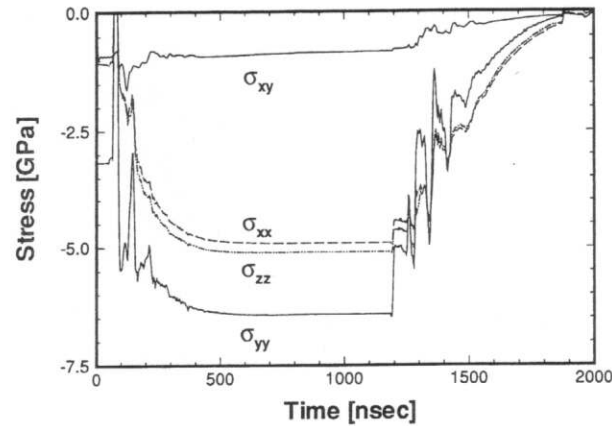
Fig. 14. History of stresses computed in an element of the AlN/AlN/Al sample located at the impact surface.

400 ns, damage is accumulated on several orientations. This damage is the result of the increase in normal and shear stresses, see Fig. 5b and c. After the normal stress has reached its maximum magnitude, the damage state remains constant in all orientations with the exception of orientation 1, see Fig. 13. As a result of this microlocalized crack growth, the numerical simulation captures the progressive reduction in transverse velocity observed experimentally. Nonetheless, upon pressure release, at approximately 1.2 μs, the model over-predicts the reduction in shear stress. This reduction of shear strength is the result of the pressure dependence of the flow mechanism, and the crack growth during unloading of the normal stress as can be seen in the plot of microcrack radius evolution, see Fig. 13. This feature suggests that if microcracking occurs, microcrack growth in unloading is inhibited by the ductile phase. Moreover, it suggests that microcracking and microplasticity may be concomitant inelastic mechanisms. High strain rate pressure-change experiments of the kind described in Espinosa and Clifton (1991) should be pursued to clarify this point.

The stress histories computed at the specimen surface are plotted in Fig. 14. The stress in the direction of propagation of the normal wave, σ_{yy}, jumps to the stress level corresponding to the impact of the AlN/AlN/Al composite against the WC/6Co anvil. Due to the presence of a gap at the impactor-specimen interface, the stress drops to zero. Subsequently, after each normal wave reverberation within the thin sample, σ_{yy} progressively increases to its maximum value of 6.9 GPa. At 1.2 μs the normal stress drops following a history similar to the initial loading. The two lateral stresses, σ_{xx} and σ_{zz}, climb initially at the same rate, but separate after 150 ns due to damage-induced anisotropy.

In view of the key role played by the frictional property of the material in the interpretation of penetration experiments, (Curran *et al.* 1993) a simulation of the pressure-shear experiment with a coefficient of friction $\mu = 0.3$ was performed. All the other parameters defining the microcracking model were kept the same. The transverse velocity history obtained from this simulation indicates that the shear resistance of the material is highly overpredicted (see Fig. 12). As in the case in which $\mu = 0.15$ is utilized, the predicted behavior upon normal unloading does not follow the experimental records for the reasons previously discussed. The observed pressure dependence is even more significant, as one may expect from the model formulation. The agreement of both velocity histories at the early stages of inelasticity suggest that if microcracking is indeed occurring, the dynamic friction coefficient may need to be formulated as being pressure, temperature and strain rate dependent. Frictional studies of the kind performed by Prakash and Clifton (1993) should be pursued to characterize the dynamic friction coefficient under conditions of high pressures and sliding rates.

6. DISCUSSION AND CONCLUDING REMARKS

The differences observed in the dynamic flow strength of the AlN/AlN/Al ceramic composite, when both normal and pressure-shear impact experiments are conducted, may

have more than one explanation. It should be noted that failure of the anvil plate due to the development of a state of pure shear loading, as could have been the case in the experiments reported by Klopp and Shockey (1991) and Curran *et al.* (1993) did not occur in this study.

One explanation of the softer behavior in pressure-shear could be that sliding occurred at the impact surface. The symmetric pressure-shear impact test conducted on WC/6Co, which is discussed in Section 5, shows that a shear stress of 1.6 GPa can be transmitted when a pressure of 10 GPa is applied to the flyer–target interface. Even when the experiment can be rationalized in terms of an inelastic response of the material, a calculation of the ratio between these shear and normal stresses gives a dynamic coefficient of friction of 0.16, which is higher than the ratio measured in the experiment reported herein for the softer AlN/AlN/Al composite. Furthermore, the lack of a decrease in shear stress upon unloading of the longitudinal wave, at 1.2 μs (see Fig. 5c), indicates the unlikelihood of slipping at the impact surface.

A second possibility is interfacial failure due to the development of localized damage. The agreement between the experimental records and the numerical simulation of the pressure-shear experiment, when the microcracking multiple-plane model is used, could be interpreted as an indication that fragmentation and interfragment sliding may be the primary mechanisms responsible for the measured shear resistance. It is well known that subsurface damage may be introduced during machining of brittle samples, or during high pressure contact of rough brittle surfaces (Buckley and Miyoshi, 1989). Assuming such damage was present or developed in the tested specimens, one may conclude that the amplitude of the transmitted shear wave was controlled by the evolution of such damage. It should be realized that the existence of surface damage in the form of subsurface microcracking, has completely different implications in the two experimental configurations under study. In the normal impact configuration, the measured decay of the elastic precursor is the result of stress relaxation during the propagation of the normal wave within the sample. By contrast, in the pressure-shear configuration, the presence of defects at the specimen surfaces may control the amplitude of the shear wave that can be transmitted through the bulk of the sample. The final result could be an *apparent* smaller shear resistance. Although the possibility of damage localization exists in the high strain rate pressure-shear experiment, the results herein reported are insufficient to support this failure mechanism.

Based on the results reported in Section 5 it is clear that the shear resistance measured in the pressure-shear configuration is much more sensitive to inelasticity and damage than the normal impact configuration. As previously shown (Fig. 13), under pressure-shear loading the inelastic shear deformation of the material is accomplished by the continuous slipping on a dominant orientation. This feature is further illustrated in Fig. 15 where shear
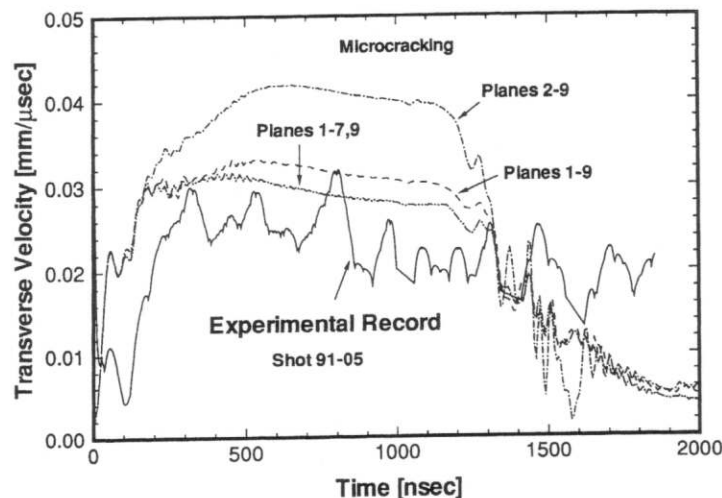

Fig. 15. Transverse velocity histories when selected orientations are removed; (i) all planes, (ii) plane 1 is excluded, (iii) plane 8 is excluded.

stress histories are plotted when selected planes are removed from eqn (6). It is observed that when plane 1 does not contribute to the inelastic strain rate, the post yield dynamic strength increases substantially. In contrast, when the second most active plane is removed, plane 8, the shear strength is further reduced because additional inelasticity is accumulated on plane 1. As a result, one may expect that softening due to damage, temperature rise, and geometrical changes, which control the dynamic shear resistance of the material, would have different significance in the two experimental configurations. The continuous deformation of the material in a microlocalized fashion (in the sense that only one orientation becomes dominant) has not been observed in the normal impact configuration. This is mainly due to the limited inelastic deformation the material experiences in this configuration. This interpretation seems the most likely among the possibilities previously discussed. It differs from the interpretation provided by Curran *et al.* (1993) in the sense that fragmentation during the early part of the pressure-shear test is not required. The important factor leading to deformation along a preferred orientation, and therefore to a softer shear resistance, is the pressure dependence of the flow mechanism. This dependence has been identified in a variety of ceramics and ceramic composites in plate impact studies (Rosenberg *et al.*, 1988; Kipp and Grady, 1989), and it constitutes an essential distinction from the flow properties of metals. Although the micromechanical formulation incorporated in the multiple-plane model is based on microcracking, the discussion equally applies to pressure dependent plastic flow along certain orientations. It should be noted that under fully compressive loading, the distinction between microcracking and microplasticity is more mathematical than physical.

Further research with the multiple-plane model based on physical mechanisms *experimentally observed*, incorporating a coupled damage-microplasticity model, seems very promising for a proper description of the behavior of brittle and quasi-brittle materials under conditions of high strain rates and pressures. The inadequacies observed in each one of the examined models could then be eliminated while preserving the key feature of shear flow along dominant orientations (deformation induced anisotropy). These formulations should use more than nine independent planes in order to obtain sufficient precision in the inelastic description of the material. Bazant and Oh (1985) found that 20 or more microplanes are necessary to properly represent anisotropic behavior.

The significance of the formulation of mathematical models that describe plastic flow, microfracture and other inelasticities in the simulation of plate impact experiments is clearly shown in this work. Although some insight about the high strain rate response of brittle and quasi-brittle materials has been gained through these numerical simulations, several uncertainties remain. These uncertainties in the interpretation of plate impact experiments may be eliminated only through the performance of microscopy studies on the tested samples. These studies would provide the bases for the formulation of physically based mathematical models. This goal has been accomplished by means of normal impact soft-recovery experiments performed at relatively low impact velocities (Clifton *et al.*, 1989; Espinosa *et al.*, 1992). Extension of the technique to higher velocities and pressure-shear experiments seems possible (Espinosa, 1992). Furthermore, a systematic study addressing the frictional properties of ceramic and ceramic composite surfaces, and damage-induced localization by performing specially designed soft-recovery experiments seems to be the only avenue for a complete correlation between the recorded velocity histories and the inferred deformation mechanisms. Fundamental understanding of these mechanisms can significantly enhance the development of new materials with special properties.

REFERENCES

Bazant, Z. P. and Gambarova, P. G. (1984). Crack shear in concrete: crack band microplane model. *J. Struct. Engng ASCE* **110**(9), 2015–2035.

Bazant, Z. P. and Oh, B. H. (1985). Microplane model for progressive fracture of concrete and rock. *J. Engng Mech. ASCE* **111**, 559.

Broberg, K. B. (1978). On transient sliding motion. *Geophys. J. R. Astronom. Soc.* **52**, 397–432.

Buckley, D. H. and Miyoshi, K. (1989). Tribological properties of structural ceramics. *Treatise Mater. Sci. and Techn.* **29**, 293–365.

Chen, C. T. and Sih, G. C. (1977). Transient response of cracks to impact in *Elastodynamic Crack Problems* (Edited by G. C. Shi), 1–58. Noordhoff, Leyden.

Chen, C. T. and Wilkins, M. L. (1976). Stress analysis of crack problems with a three-dimensional, time dependent computer program. *Int. J. of Fracture* **12**, 607–617.

Clifton, R. J. Raiser, G. Ortiz, M. and Espinosa, H. D. (1989). A soft recovery experiment for ceramics. *Proc. of 1989 APS Conf. on Shock Compression of Condensed Matter*, 1989, pp. 437–440.

Curran, D. R. Seaman, L., Cooper, T. and Shockey, D. A. (1993). Micromechanical model for comminution and granular flow of brittle material under high strain rate. Application to penetration of ceramic targets. *Int. J. Impact Engng* **13**, 53–83.

Espinosa, H. D. (1989). Finite element analysis of stress induced damage in ceramics. M.Sc. Thesis. Brown University, Providence, RI.

Espinosa, H. D. (1992). Micromechanics of the dynamic response of ceramics and ceramic composites. Ph.D. Thesis. Brown University, Providence, RI.

Espinosa, H. D. and Clifton, R. J. (1991). Plate impact experiments for investigating inelastic deformation and damage of advanced materials. *Symp. on Experiments in Micromechanics of Fracture-Resistant Material* (Edited by Kim K. S.), pp. 37–56. ASME Winter Annual Meeting.

Espinosa, H. D. Raiser, G. Clifton, R. J. and Ortiz, M. (1992). Experimental observations and numerical modeling of inelasticity in dynamically loaded ceramics. *J. Hard Mater.* **3**, 285–313.

Freund, L. B. (1972a). Crack propagation in an elastic solid subjected to general loading. I. Constant rate of extension. *J. Mech. Phys. Solids* **20**, 129–140.

Freund, L. B. (1972b). Crack propagation in an elastic solid subjected to general loading. II. Nonuniform rate of extension. *J. Mech. Phys. Solids* **20**, 141–152.

Freund, L. B. (1990). *Dynamic Fracture Mechanics*. Cambridge University Press, Cambridge.

Freund, L. B. and Hutchinson, J. W. (1985). High strain-rate crack growth in rate-dependent plastic solids. *J. Mech. Phys. Solids* **33**, 169.

Hagege, S. Ishida, Y. and Tanaka, S. (1988) HVEM and HREM of interfaces in AlN ceramics. *J. Phys.* **C5**, 189–194.

Johnson, G. R., Holmquist, T. J. Lankford, J. Anderson, C. E. and Walker, J. (1990). A computational constitutive model and test data for ceramics subjected to large strains, high strain rates, and high pressures. Final Technical Report on Optimal Task I, DOD Contract No. DE-AC04-87AL-42550.

Ju, J. W. (1992). On algorithmic tangent moduli for a class of viscoplastic models. In *Plastic Flow and Creep*, Vol. 135, pp. 67–78. ASME, AMD.

Ju, J. W. and Lee, X. (1991a). On three dimensional self-consistent micromechanical damage models for brittle solids. Part I: tensile loadings. *Journal of Engng. Mech., ASCE* **117**, 1495–1514.

Ju, J. W. and Lee, X. (1991b). On three dimensional self-consistent micromechanical damage models for brittle solids. Part II: compressive loadings. *J. Engng Mech. ASCE* **117**, 1515–1536.

Kachanov, M. (1980). Continuum Model of Medium with Cracks. *J. Engng Mech. Div. ASCE* **106** (EM5), 1039–1051.

Kipp, M. and Grady, D. (1989). Shock compression and release in high-strength ceramics. *Sandia Rep.* SAND89–1461.

Klopp, R. W. and Shockey, D. A. (1991). The strength behavior of granulated silicon carbide at high strain rates and confining pressure. *J. Appl. Phys.* **70**, 7318–7326.

Leroy, Y. and Ortiz, M. (1988). Finite element analysis of strain localization in frictional materials. *Int. J. Num. Anal. Meth. Geom.* **12**, 1–22.

Nagelberg, A. S. (1989). The effect of processing parameters on the growth rate and microstructure of Al_2O_3/metal matrix composites. *Mater. Res. Soc. Proc.* **155**, 275–282.

Needleman, A. (1988). Material rate dependence and mesh sensitivity in localization problems. *Comput. Meth. Engng* **67**, 69.

Ortiz, M. and Popov, E. P. (1985). Accuracy and stability of integration algorithms for elastoplastic constitutive equations. *Int. J. Numer. Meth. Engng* **21**, 1561–1576.

Prakash, V. and Clifton, R. J. (1993). In *Experimental Techniques in the Dynamics of Deformable Solids* (Edited by K. T. Ramesh), Vol 165, pp. 33–48. ASME, AMD New York.

Rajendran, A. M. (1992). High strain rate behavior of metals, ceramics, and concrete. *Air Force Report WL-TR-92-4006*. Wright-Patterson Air Force Base, OH.

Rosenberg, Z. and Partom, Y. (1985). Longitudinal dynamic stress measurements with in-material piezoresistive gauges. *J. Appl. Phys.* **58**, 1814–1818.

Rosenberg, Z., Brar, N. S. and Bless, S. J. (1988). Elastic precursor decay in ceramics as determined with manganin stress gauges. *J. Phys.* **C3**, 707.

Rosenberg, Z. Brar, N. S. and Bless, S. J. (1991). Dynamic High Pressure properties of AlN ceramic as determined by flyer plate impact. *J. Appl. Phys.* **70**, 167–171.

Sandler, I. S. and Wright, J. P. (1984). Strain-softening. *Theoretical Foundations for Large Scale Computations of Nonlinear Materials Behavior* (Edited by S. Nemat-Nasser, R. J. Asaro and G. A. Hegemien), p. 285. Martinus Nijhoff.

Seaman, L. and Dein, J. L. (1983). Representing shear band damage at high strain rates. *Proceeding of the IUTAM Symposium on Nonlinear Deformation Waves*. Tallin, Estonia; published by Springer, Berlin.

Seaman, L. Curran, D. R. and Crewdson, R. C. (1978). Transformation of observed crack traces on a section to true crack density for fracture calculations. *J. Appl. Phys.* **49,** 5221.

Simo, J. C., Kennedy, J. G. and Govindjee, S. (1988). Non-smooth Multisurface plasticity and viscoplasticity. Loading/unloading conditions and numerical algorithms. *Int. J. Numer. Meth. Engng* **26,** 2161–2185.

Shockey, D. A. Marchand, A. H. Skaggs, S. R. Cort, G. E. Burkett, M. W. and Parker, R. (1990). Failure phenomenology of confined ceramic targets and impacting rods. *Int. J. Impact Engng* **9,** 263–275.

Sneddon, I. N. (1946). The distribution of stress in the neighborhood of a crack in an elastic solid. *Proc. R. Soc.* (*Lond.*) **A187,** 229–260.

Tong, W. (1991). Pressure-shear impact investigation of strain-rate history effects in OFHC copper. PhD Thesis. Brown University, Providence, RI.

Willis, I. R. (1968). The stress field around an elliptical crack. *Int. J. Engng. Sci.* **6,** 253–263.